Acta Materialia 189 (2020) 299–305

Contents lists available at ScienceDirect

Acta Materialia

journal homepage: www.elsevier.com/locate/actamat

Full length article

# Anisotropic thermal conductivity tensor of $\beta$-$Y_2Si_2O_7$ for orientational control of heat flow on micrometer scales

David H. Olson[a], Valentina Angelici Avincola[b], Cory G. Parker[b], Jeffrey L. Braun[a], John T. Gaskins[a], John A. Tomko[b], Elizabeth J. Opila[b], Patrick E. Hopkins*[,a,b,c]

[a] Department of Mechanical and Aerospace Engineering, University of Virginia, Charlottesville, Virginia 22904, USA
[b] Department of Materials Science and Engineering, University of Virginia, Charlottesville, Virginia 22904, USA
[c] Department of Physics, University of Virginia, Charlottesville, Virginia 22904, USA

ARTICLE INFO

*Article History:*
Received 8 October 2019
Revised 21 January 2020
Accepted 17 February 2020
Available online 22 February 2020

*Keywords:*
Thermal conductivity
Anisotropy
Yttrium disilicate
Environmental barrier coating
Time-domain thermoreflectance mapping

ABSTRACT

The ability to relate the spatially-varying anisotropy of thermal conductivity to crystal structure would provide a foundational advance in our understanding of length-scale dependent heat flow. The challenge, however, is in determining the thermal conductivity tensor in polycrystalline systems with anisotropic crystal structures. Apparent isotropic thermal conductivity in randomly oriented polycrystals with anisotropic properties break down at length scales approaching the grain size. As a result, a measured isotropic thermal conductivity from the macroscale perspective may differ greatly from that measured at the nano or microscale, and thus microscale anisotropic heat flow could underlie a seemingly isotropic thermal conductivity. We experimentally investigate the anisotropic thermal conductivity in polycrystalline beta-phase yttrium disilicate ($\beta$-$Y_2Si_2O_7$). This is achieved through micrometer-resolution thermal conductivity mapping correlated to the phase and orientation of individual grains, allowing for the determination of the thermal conductivity tensor of $\beta$-$Y_2Si_2O_7$. Our results are the first to reproduce the thermal conductivity tensor of a polycrystalline system with anisotropic crystal structure based on the spatial distribution of thermal conductivity.



The harsh conditions experienced by coatings in extreme environments intensifies the rate at which materials fail. For example, the localized power densities and associated temperature increases in high temperature chemically reactive atmospheres can give rise to hot spots and large thermal gradients [1–3] where resultant thermal expansion and material deformation [4–6] can promote coating failure via cracking, delamination, oxidation, corrosion and spallation [7–10]. Due to the thermochemical and thermomechanical constraints on materials in these environments, the phase space of materials available for use in these extreme atmospheres is limited. SiC-based turbine components in combination with an environmental barrier coating (EBC) have been shown as promising material systems for implementation as turbine engine components [9,11]. Due to the intense combustion environments in which these material systems operate, EBCs possessing high water-vapor resistance, low contrast in thermal expansion coefficient to adjacent and subsurface materials, and chemical and mechanical stability at high temperatures make them attractive for the protection of subsurface materials [12]. Rare earth (RE) silicates have been shown to exhibit the above qualities [13,14], with the capacity to withstand temperatures up to and higher than 1316 °C for thousands of hours [15]. These combined characteristics have brought RE silicates to the forefront of technological relevance in the search for EBCs for turbine component protective coatings in extreme environments.

Yttrium-based silicate coatings have been identified as promising candidates for EBCs. Compared to conventionally used barium strontium aluminosilicate, yttrium silicates exhibit improved oxidation and corrosion resistance, all while maintaining high temperature thermomechanical stability [16]. The comparable coefficient of thermal expansion (CTE) of $\gamma$-$Y_2Si_2O_7$ to those of SiC and mullite make it a suitable EBC in addition to its resistance properties [13,17], offering further relief from the stresses arising from thermal cycling [16,18–21]. $Y_2Si_2O_7$ continues to offer itself as a promising candidate for EBC applications.

The thermal conductivity associated with these silicates is a critical property that needs to be taken into consideration when designing EBCs, as this ultimately dictates the material's heat spreading ability, resultant internal energy densities, and local temperature rises. Various works have examined the thermal conductivity of yttria-based silicates in their bulk form with values ranging from 0.161 to 4.91 W $m^{-1}$ $K^{-1}$, depending on the porosity of the system [17,21–24]. Thermal conductivity for these reported values generally represent an average thermal conductivity of a polycrystalline, possibly multi-phase

* Corresponding author.
*E-mail address:* phopkins@virginia.edu (P.E. Hopkins).

https://doi.org/10.1016/j.actamat.2020.02.040
1359-6454/

system. For example, in all of the aforementioned reports of yttria-based silicate thermal conductivity, laser-flash was employed, thus sampling the average thermal diffusivity over the entire volume of the sample. These measurements cannot isolate the microstructural or anisotropic influences that different grains have on thermal transport in the sample, especially when the structure is monoclinic as is for the majority of the rare earth monosilicates and some disilicates. Clarke *et al.* [22] have shown that at high temperatures, the thermal conductivity of various disilicates can achieve exceptionally low values, reaching the theoretical minimum limit to thermal conductivity [25]. Additionally, they demonstrate that the thermal conductivity of Y-, Yb-, and Lu-based disilicates can theoretically be anisotropic. For these complicated systems, an anisotropic thermal conductivity tensor dictating the flow of heat is not to be ignored, and has the potential to largely influence EBC applications at the macroscale.

The challenge, however, is in determining the thermal conductivity tensor in this polycrystalline system with an anisotropic crystal structure. At large length scales, much larger than the characteristic grain sizes in a material, non-textured polycrystalline materials with anisotropic crystal structures yield an isotropic thermal conductivity. This thermal conductivity isotropy breaks down at the length scale of the energy carriers, in our case, the mean free paths of the phonons. Thus, while the thermal conductivity may appear isotropic at macroscopic scales, spatially varying temperature rises and local hot spots can occur that defy this isotropic assumption, since the microscopic nature of the crystal structure in the grains, which is anisotropic, will dictate phonon scattering and local temperature rises. While structural characterization techniques can clearly resolve differences in local crystal orientation and phases (e.g., electron-backscatter diffraction), thermal measurement techniques have not been afforded the luxury of measuring local anisotropy variation from grain to grain over length scales consisting of several grains. This has led to a void in our understanding of not only how the local thermal conductivity of anisotropic polycrystalline samples relates to the more globally-averaged values, but also leaves several theoretical treatments of thermal conductivity anisotropy in crystal systems of lower symmetry unvetted.

In this work, we experimentally measure the thermal conductivity tensor of $\beta$-$Y_2Si_2O_7$ by conducting an areal map of the thermal conductivity of polycrystalline $\beta$-$Y_2Si_2O_7$ with $\sim$ 2 μm resolution. Locally probing grains and correlating their crystalline orientations to electron-backscatter diffraction (EBSD) data allows us to measure the orientation-dependence of heat conduction as quantified by the thermal conductivity. In doing so, we determine the thermal conductivity tensor of the monoclinic $\beta$-$Y_2Si_2O_7$ system. We find that $\beta$-$Y_2Si_2O_7$ is anisotropic, with an $\sim$ 40% change in thermal conductivity from its most to least-insulating orientations. This strong variation in thermal conductivity of $\beta$-$Y_2Si_2O_7$ based on grain orientation, which is driven by the naturally large anisotropy in the crystal, has major implications with regard to predicting mechanisms of failure based on local thermal strains, and suggests the potential to preferentially texture polycrystalline EBCs to enhance, restrict, and/or direct heat flow.

An atmospheric air plasma spray (APS) process was implemented to fabricate a bulk $Y_2Si_2O_7$ specimen. The APS process is a non-equilibrium line of sight thermal spray process, in which a plasma is created using a high amperage anode with either hydrogen or helium. This plasma has a core temperature of $\sim$ 20,000 K with a steep temperature gradient. $Y_2Si_2O_7$ powders are fed into the torch and ejected into the plasma using high flow rates of an inert gas on the order of hundreds of cubic feet per hour. The inhomogenous heating of the powders and variation in powder size results in a heterogeneous mixture of non-equilibrium phases in the coating. A post-anneal of 1200 °C for 120 hours in ambient conditions was performed in order to finalize the heterogeneous mixture of the system. The sample is further characterized via scanning electron-microscopy and EBSD for local variations in phase and orientation using a Helios UC G4 Dual Beam FIB-SEM. X-ray diffraction was performed using a Panalytical Empyrean XRD.

The post-annealed bulk $Y_2Si_2O_7$ specimen obtained is polycrystalline with microstructural features on the order of $\sim$ 5 μm. Representative X-ray diffraction (XRD) of the sample can be seen in Fig. 1(a), which shows that the sample is a multi-phase system consisting of $\gamma$ and $\beta$ phases of $Y_2Si_2O_7$ as well as $Y_2SiO_5$. Representative SEM and EBSD micrographs of select grains are shown in Figs. 1(b) and (c). The EBSD orientation image shows the varying orientations of grains present in Fig. 1(b). Both $\gamma$- and $\beta$-$Y_2Si_2O_7$ are present in this region, as shown via EBSD phase micrographs in the Supplementary Information. Because of the predominantly $\beta$ phase $Y_2Si_2O_7$ in our EBSD maps, we choose to analyze anisotropic thermal conductivity solely in this phase. EBSD phase micrographs for all regions analyzed in this work can be found in the Supplementary Information. We further selectively examine areas via ESBD to verify crystalline orientations of various grains in different regions of the sample. Grains of interest can be seen in representative SEM and EBSD micrographs in Fig. 2. We note that various orientations of the disilicate are present, with grain sizes on the order of $\sim$ 5 μm. The lattice parameters of $\beta$-$Y_2Si_2O_7$ are a = 6.8691 Å, b = 8.960 Å, c = 4.7168 Å, and $\beta$ = 101.73° [26]. In order to facilitate spatial thermal conductivity mapping via time-domain thermoreflectance (TDTR), we deposit an aluminum transducer with nominal thickness of 80 nm via electron-beam deposition.

TDTR and similar pump-probe metrologies are widely used and vetted in the literature [27–29], and is the technique we use to characterize local variations in the thermal conductivity of $\beta$-$Y_2Si_2O_7$. In our experimental configuration, we spectrally separate the output of an 80 MHz Ti:Sapphire oscillator centered at 808.5 nm into pump and probe paths. The pump path is electro-optically modulated at 8.4 MHz, and creates a frequency-dependent heating event at the sample surface. The probe is mechanically delayed in time and monitors the thermoreflectance at the sample surface. The cooling curve is compared to the radially symmetric heat diffusion equation to extract the thermal conductivity.

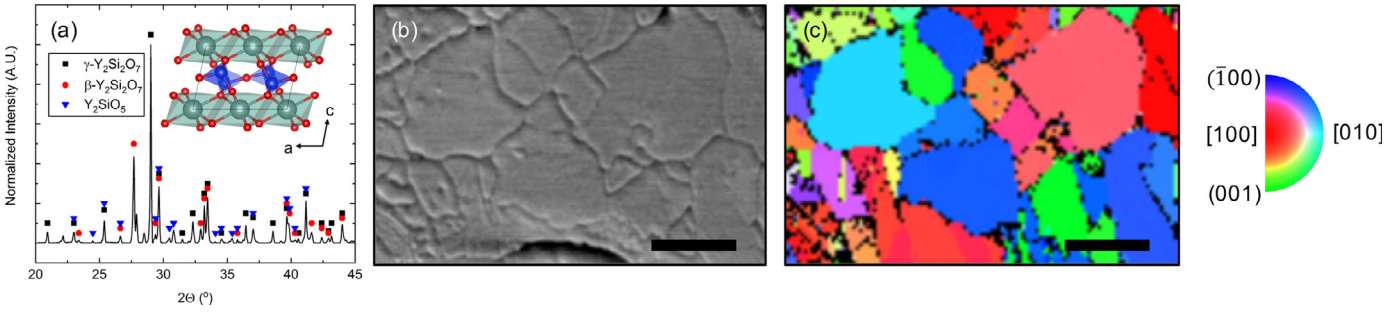


**Fig. 1.** (a) X-ray diffractogram of the sample of interest, confirming the presence of $Y_2SiO_5$ and $\gamma$- and $\beta$-phases of $Y_2Si_2O_7$. (b) Representative SEM of select grains for reference. (c) Inverse pole figure Z (IPF Z) electron backscatter diffraction orientation micrograph, showing the differing orientations of grains in (b). See Supplementary Information for EBSD phase micrograph of the same region. The scale bar in (b) and (c) is 5 μm.

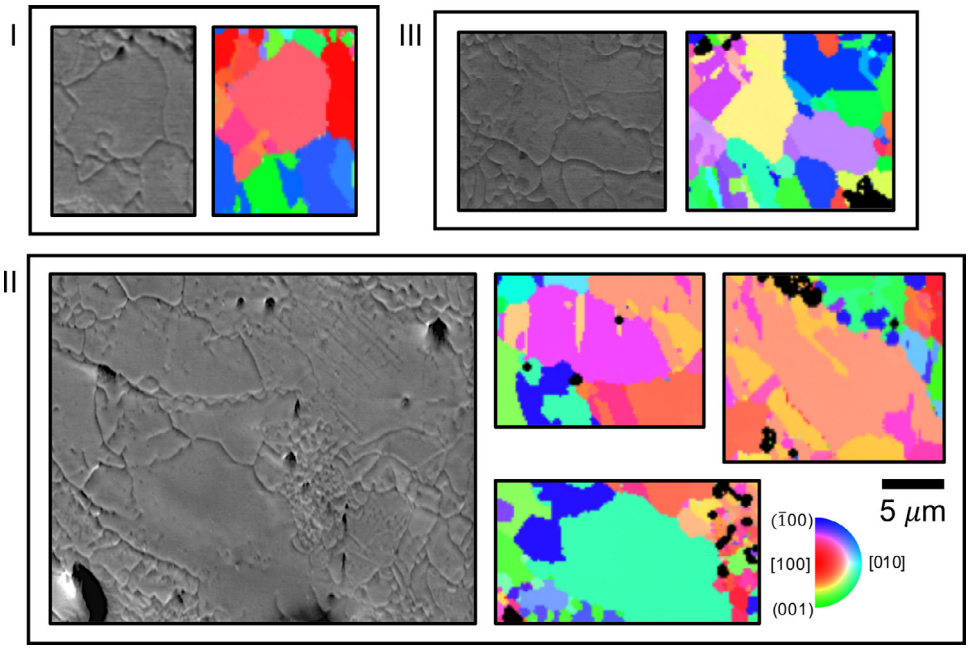


**Fig. 2.** SEM and inverse pole figure (IPF) Z EBSD micrographs of the grains of interest. Regions are denoted by Roman numerals in the top left of each box. The IPF Z key demonstrates orientation of the grains in EBSD micrographs. Note that all EBSD micrographs contain grains with those of similar and different orientations.

Typically, optical pump-probe techniques utilizing high modulation frequencies are relatively insensitive to in-plane thermal conductivity compared to cross-plane conductivity [27]. At low modulation frequencies, TDTR and frequency-domain thermoreflectance can gain increased sensitivities to anisotropy in the thermal conductivity tensor. Various methods have been proposed for measurements of this anisotropy, including beam-offset [30–32] and elliptic-beam techniques [33,34]. While versatile, these methods are highly sensitive to the ellipticity of the beam and the repeatability of the measured FWHM of the cross-correlation of the pump and probe in beam-offset approaches [31]. Additionally, these methodologies generally require the use of a low thermal conductivity transducer, such as NbV, to enhance sensitivity to in-plane transport in the underlying material and reduce uncertainties in the extracted parameters. For elliptic-beam techniques, either the beam or specimen must be systematically rotated until the measurement axis is along the axis of interest, which introduces additional uncertainties into the beam size and/or specimen orientation. Further difficulties lie in the interpretation of EBSD in-plane orientations, which are necessary to extract in-plane thermal conductivities for offset and elliptic beam techniques. Precise knowledge of sample orientation relative to the EBSD data is required for accurate determination of in-plane thermal conductivity. Neither the measurement nor the post-processing associated with these measurements are trivial. This further demonstrates the power of methodologies capable of extracting the cross-plane thermal conductivity for grains of varying orientation to extract the thermal conductivity tensor of a material system.

Using a typical thermal model for a two layer system (i.e., 80 nm Al transducer on a substrate), TDTR is capable of measuring both the thermal boundary conductance between the Al transducer and the underlying media, as well as the thermal conductivity of the media. An example cooling curve used to extract these two parameters for a select grain in Region II can be found in the Supplementary Information. To perform thermal conductivity mapping, however, the thermal boundary conductance should be adequately known, as the data from a single pump-probe delay time is used to extract the thermal conductivity of the underlying material. We take numerous full TDTR scans across all regions of interest and fit for the thermal conductivity of the disilicate and the thermal boundary conductance between the disilicate and the underlying material. At a modulation frequency of 8.4 MHz, we maintain one-dimensionality and are sensitive to primarily the cross-plane thermal conductivity and thermal boundary conductance, leaving any influence from in-plane transport to be negligible. We find that the thermal boundary conductance in regions I, II, and III are 43 $\pm$ 2, 56 $\pm$ 3, and 41 $\pm$ 3 MW m$^{-2}$ K$^{-1}$, which reflect the measured conductance from multiple full TDTR scans in a given region. These values are then used in our sensitivity analysis for the determination of our pump-probe delay time for the mapping procedure, which is further discussed in the Supplementary Information. In our measurements, the RMS pump/probe radii is $\sim$ 1.6 μm, and is determined by fitting the spot size using a sapphire reference sample. We calculate uncertainties based on the work of Wei *et al.* [35], with errors of 2.5% in the pump/probe radii, 6% in the thermal conductivity of the Al transducer, 2.5% in the thickness of the Al transducer, 5% in the boundary conductance at the Al/disilicate interface, and 5% in the volumetric heat capacity of the disilicate. At this modulation frequency, we take into account an error in phase of 0.2 mrad. Uncertainty analysis for all grains analyzed in this work can be found in the Supplementary Information.

To facilitate thermal conductivity mapping of the specimen, we mount it on a 3-axis stage, with motors along the sample orientation having a bidirectional repeatability of $<$ 0.5 μm and a closed-loop piezo motor controlling the focal plane of the sample. We orient the stage in such a way such that movements along the sample surface result in no appreciable change in focus. The pump/probe delay time is chosen, as previously discussed, such that we maximize our sensitivity to the thermal conductivity of the disilicate. The sample is then rastered over a region of interest to probe the thermal conductivity as a function of microstructural variation across the sample. Unless otherwise specified, the step size in the thermal conductivity micrographs is 0.25 μm.

The spatial resolution of the measurement is affected by a multitude of parameters beyond the $1/e^2$ pump/probe radii. These include the modulation frequency of the pump, the thermal conductivity and thickness of the Al transducer, the thermal conductivity of the underlying disilicate, and the thermal conductance at the Al/disilicate interface. At the modulation frequency with which we perform our experiment (8.4 MHz), the in-plane thermal penetration depth, and thus the spatial resolution of the measurement, is greatly diminished as a result of the predominantly one-dimensional heating event. In general, an increase

in transducer thickness and thermal conductivity will result in increased in-plane heat spreading, and extend the spatial resolution for a fixed modulation frequency. While the thermal penetration depth in the high-frequency limit (i.e., $\sqrt{\kappa/\pi Cf}$) has often been used to estimate in-plane thermal penetration depths, this parameter must be numerically determined to account for geometrical considerations of the material system [35,36]. The in- and cross-plane thermal penetration depths as a function of modulation frequency can be found in the Supplementary Information, where we show that the in-plane thermal penetration depth for a system of this geometry follows $\sim f^{-0.1}$ in the high-frequency limit. Based on the parameters of our system, we find that the in-plane thermal penetration depth, and thus the spatial resolution of our experiment, is $\sim 1.1$ μm.

Thermal conductivity micrographs of the three regions of interest are shown in Fig. 3. The thermal conductivity ranges from 5 to 7 W m$^{-1}$ K$^{-1}$ in the grains of interest. Regions in which the probe beam is diffusely scattered create artifacts in our acquired signal, and therefore cannot be analyzed with confidence. To overcome these artifacts, we choose to only analyze regions in which the probe is highly reflective so that they do not erroneously impact our results. The specific details are discussed further in the Supplementary Information, along with reflectivity micrographs of the surface of each region. At these length scales, we do not expect a reduction in the thermal conductivity near grain boundaries to influence our results, as this is only to be expected in materials with mean free paths greater than our spot sizes, such as diamond [37]. Maps corresponding to the uncertainty in thermal conductivity can be found in the Supplementary Information, along with higher-resolution micrographs of Regions II.

The stereographic projection of the measured values with respect to the monoclinic system is shown can be found in Fig. 4(a), where the dots represent the orientations of the grains analyzed for their thermal conductivity. The error in the measured thermal conductivity values is on the order of $\sim 20\%$, as an error of 2.5% in the spot size propagates into an error of $\sim 15\%$ in thermal conductivity. The exact measured values and uncertainties for each grain are tabulated in the Supporting Information. We further examine the thermal conductivity from a continuum approach, extracting the thermal conductivity tensor of the system.

The thermal conductivity tensor of a monoclinic system takes the form [38]

$$\tilde{\mathbf{K}} = \begin{bmatrix} \kappa_{xx} & 0 & \kappa_{xz} \\ 0 & \kappa_{yy} & 0 \\ \kappa_{xz} & 0 & \kappa_{zz} \end{bmatrix},$$

where $\kappa_{xx}$ and $\kappa_{yy}$ are thermal conductivities measured along the [100] and [010] directions, respectively, and $\kappa_{zz}$ is the thermal conductivity measured orthogonal to [100] and [010], $\beta$-90 degrees from the [001] direction, where $\beta$ is the angle between the [100] and [001] directions. We will refer to the [100] and [010] directions as $\hat{x}$ and $\hat{y}$, respectively, and the orthogonal to the two as $\hat{z}$. One can explicitly derive the angular dependence of thermal conductivity of a monoclinic system on $\theta$ and $\phi$:

$$\kappa(\theta,\phi) = \kappa_{xx}\sin^2\phi\cos^2\theta + \kappa_{yy}\sin^2\phi\sin^2\theta + \kappa_{zz}\cos^2\phi + 2\kappa_{xz}\sin\phi\cos\theta\cos\phi. \quad (1)$$

In this equation, $\phi$ is the angle from the $\hat{z}$ direction, and $\theta$ is the angle from the $\hat{x}$ direction to the projection of the grain orientation onto the $\hat{x}$–$\hat{y}$ plane. The full derivation can be found in the Supplementary Information.

As the orientation of the grains are known from EBSD, a least-squares minimization of Eq. (1) allows us to recover the components of the thermal conductivity tensor. The thermal conductivity tensor of $\beta$-$Y_2Si_2O_7$ takes the final form

$$\tilde{\mathbf{K}} = \begin{bmatrix} 7.2\pm1.7 & 0 & -0.2\pm0.1 \\ 0 & 5.3\pm1.4 & 0 \\ -0.2\pm0.1 & 0 & 5.3\pm1.6 \end{bmatrix} \text{W m}^{-1}\text{ K}^{-1},$$

where the uncertainties include the uncertainties in the measured parameters as well as the 95% confidence interval of the best fit to Eq. (1). It is important to note that the appearance of $\kappa_{xz}$ is due to the deflection of the monoclinic from the Cartesian coordinate system, and that the determinant of the thermal conductivity tensor must be positive so as to be in congruence with the second law of thermodynamics. The negative thermal conductivity of $\kappa_{xz}$ suggests that a temperature gradient imposed in the $\hat{x}$ direction would result in a heat flux in the -$\hat{z}$ direction, and vice versa. A rotation of $\pi$ about the $\hat{z}$ direction results in a positive $\kappa_{xz}$ component.

To better visualize the thermal conductivity tensor of this system as it relates to the structure, we plot these thermal conductivities as a stereographic projection of the crystal system, shown in Fig. 4(b). We note that the thermal conductivity along the [100] and [$\bar{1}$00] directions are identical in thermal conductivity due to the symmetry of the monoclinic system. We also find that the thermal conductivity along the [001] and [010] directions are both smaller in magnitude than the [100] direction. The minimum attainable thermal conductivity occurs in the [010] direction. Overall, the directional-dependent thermal

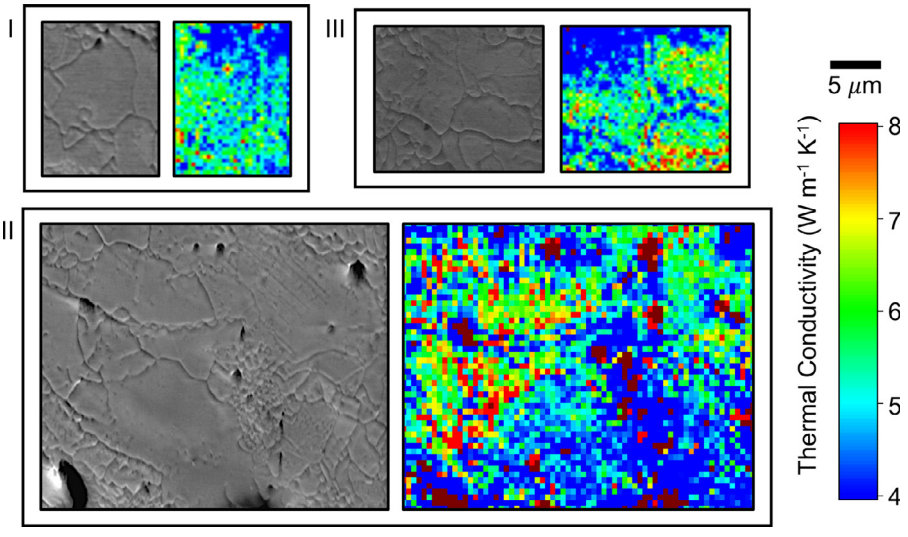


**Fig. 3.** Thermal conductivity maps for each of the three regions examined. The step size in regions I and III is 0.25 μm, while that in region II is 0.5 μm. Maps with finer resolution of grains presented in Region II can be found in the Supplementary Information.

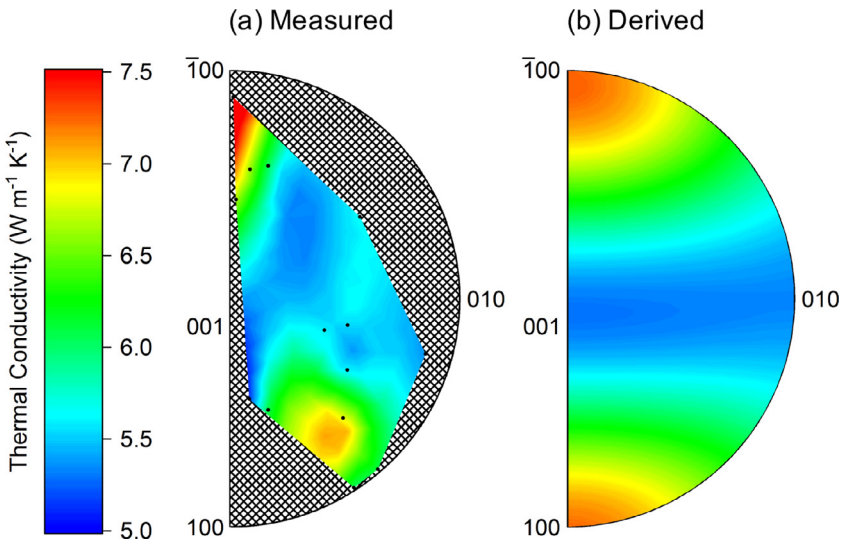


**Fig. 4.** (a) The measured thermal conductivity from the three selected regions, plotted as a stereographic projection of the monoclinic crystal. The black data points represent measured data from each of the three regions. Hashed regions indicate orientations of grains that we are not present in the three regions analyzed. (b) Thermal conductivity orientation map of $\beta$-$Y_2Si_2O_7$ based on the derived thermal conductivity tensor, represented as an inverse pole figure of the monoclinic structure.

conductivity as represented in Fig. 4(b) is in good agreement with our measured data. Tabulated values from Eq. (1) using our extracted thermal conductivity tensor can be found in Table S2 of the Supplementary Information. In Fig. 5, we show the (a) thermal conductivity magnitude from Eq. (1) and (b) the representation ellipsoid defined by

$$1 = K_{ij}x_i x_j, \tag{2}$$

where $x_i$ and $x_j$ are the coordinates of the system. The radius of the thermal conductivity ellipsoid in Fig. 5(b) for a given coordinate pair is the inverse of the root of the thermal conductivity magnitude for that coordinate pair (i.e., $\kappa^{-1/2}$, where $\kappa$ is the thermal conductivity for some $x_i$ and $x_j$).

From the kinetic theory of gasses, the phonon contribution to thermal conductivity can be approximated as $\kappa = \frac{1}{3}Cv^2\tau$ [39]. In this equation, $C$ is the volumetric heat capacity, $v$ is the group velocity of thermal carriers, and $\tau$ is the scattering rate. We take $C$ to be identical for each of the crystalline orientations, which is reasonable because the volumetric heat capacity of a given system takes no directional dependence. If the directional-dependence to the thermal conductivity is dictated by the group velocity of the thermal carriers, then we should see variations in this parameter based on calculated velocities from the elastic constants of the system. Using elastic constants from literature [40], the Christoffel equation can be solved for an arbitrary orientation in the system to extract the group velocities of longitudinal and transverse modes [41]. The Debye velocity, $v_D$, can then be calculated as,

$$\frac{3}{v_D^2} = \frac{1}{v_l^2} + \frac{1}{v_{t,1}^2} + \frac{1}{v_{t,2}^2}, \tag{3}$$

where $v_l$ is the speed of the longitudinal mode, and $v_{t,1}$ and $v_{t,2}$ are the speeds of the two transverse modes. We find $v_D$ to be $\sim$5500, $\sim$4400, and $\sim$5300 m/s along the [100], [010], and [001] directions, respectively. Steps to solve the Christoffel equation can be found in the Supplementary Information. Between the [010] and [100] directions, good agreement is found in the trend between the calculated Debye velocities and thermal conductivity, whereby an increase in the thermal conductivity is observed for increasing $v_D$. However, the thermal conductivity along the [010] and [001] directions are identical despite having different carrier velocities along these directions. Thus, we attribute the observed changes in thermal conductivity to the scattering rate, $\tau$, arising from the differing atomic

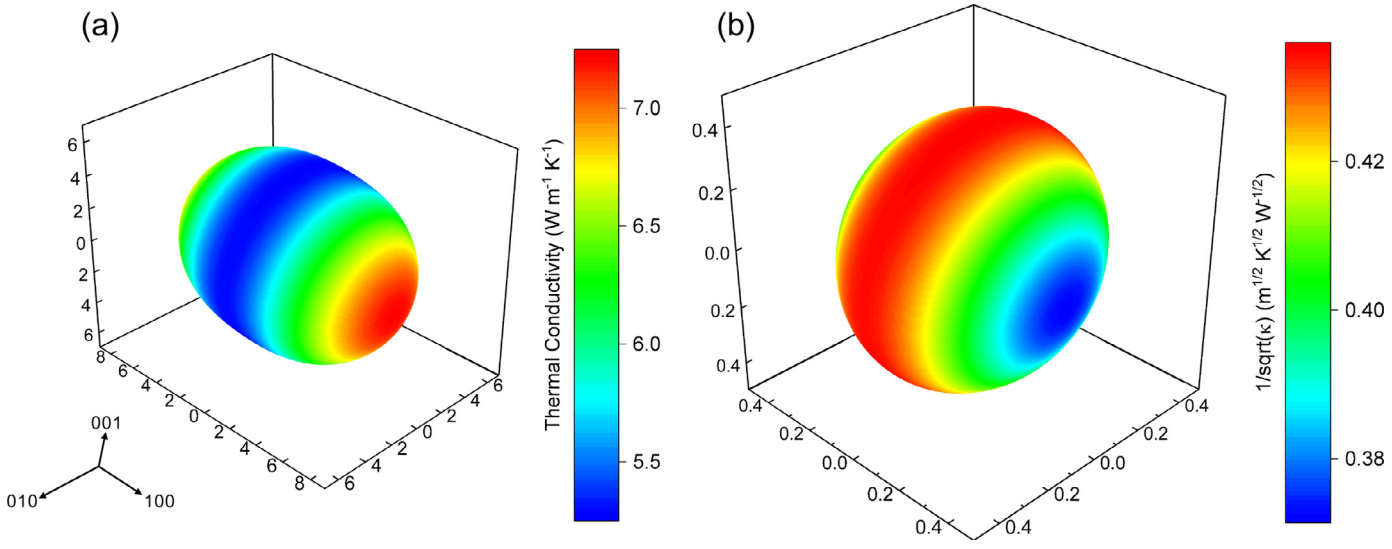


**Fig. 5.** Representation quadrics of the (a) thermal conductivity magnitude and (b) thermal conductivity ellipsoid of $\beta$-$Y_2Si_2O_7$.

environments along these crystalline directions. We present a visual representation of these differing crystalline orientations in the Supplementary Information.

Very few works in the literature have experimentally examined the anisotropic thermal conductivity of $\beta$-$Y_2Si_2O_7$. Zhou *et al.* [42] and Tian *et al.* [40] both presented experimental measurements of thermal diffusivity via the laser-flash method. In both previous works, heat capacity was confirmed independently, either by differential scanning calorimetry (DSC) or by employing the Neumann-Kopp rule as an approximation based on the constituents of the system. Regardless, both previous works describe the thermal conductivity of a bulk system, where microstructural effects and anisotropy are averaged to determine a single thermal conductivity. Furthermore, Tian *et al.* [40] have determined the anisotropic minimum thermal conductivity based on the Debye approximation in the high-temperature limit, showing a two-fold change in thermal conductivity based on crystalline orientation. The representation quadric of the thermal conductivity determined in our work is inconsistent with that obtained in Ref. [40]. They determine the directional dependence of the thermal conductivity from the anisotropic velocity as obtained from the anisotropic Young's modulus. However, this directional dependence is derived from the fourth-rank elasticity tensor, in which four extrema are possible for a given plane. Interpretation of the thermal conductivity in this manner is inconsistent with the second-rank nature of the thermal conductivity tensor in which just two extrema are possible for a given plane, the values of which reflect the eigenvalues to the in-plane thermal conductivity tensor for that plane.

Our values are higher than those found in literature for room temperature measurements; however, we can attribute the differences in our results to the measurement technique. For polycrystalline samples measured via laser flash, an average thermal conductivity of all crystalline directions and polymorphs is determined. One can define an effective thermal conductivity related to the determinant of the tensor determined as $\kappa_{\text{eff}} = \sqrt[3]{\det(\tilde{\mathbf{K}})}$, where the cube root arises due to the dimensionality of the system. For our results, we find that $\kappa_{\text{eff}} = 5.9 \pm 1.1$ W m$^{-1}$ K$^{-1}$, which one would expect to recover in the event that the measurement technique is sensitive to all components of the thermal conductivity tensor, or in the limit that the measurement spot size in TDTR is much larger than the mean grain size in a non-textured, polycrystalline $\beta$-$Y_2Si_2O_7$ sample and the extracted parameter is not influenced via the inclusion of grain boundaries or other extrinsic effects. Our results are the first to report on spatially measuring thermal conductivity via TDTR to reproduce the thermal conductivity tensor of an anisotropic material system, specifically that of $\beta$-$Y_2Si_2O_7$.

Based on the similarity of the elastic constants of $\beta$-$Y_2Si_2O_7$ to other monoclinic disilicates used in the coatings community (Yb, Lu), we can expect similar trends in thermal conductivity based on these elastic constants. Ultimately, this suggests the need to better understand texturing techniques along directions of low thermal conductivity, which may allow for tailoring heat flow in order to enhance the performance of gas turbine engines. Anisotropic thermal conductivities in these material systems can provide several key advantages in bettering these efficiencies. Beyond creating a larger temperature gradient between hot engine gasses and the underlying turbine blade, improved lateral heat flow along the surface of the coating will allow for more convective cooling near the surface. Indeed, numerical simulations have shown the potential for hot spot generation on gas turbine blades, and these findings offer a mitigation strategy toward solving this problem [2].

In summary, we fabricated polycrystalline $Y_2Si_2O_7$ that contains various polymorphs of the disilicate, as well as yttria. Conventional methods used to determine the thermal conductivity of these materials rely on bulk sample measurements, which do not yield insight into the microstructurally dependent thermal conductivity of individual grains, instead averaging the thermal conductivity of the entire system. We show that TDTR is capable of spatially separating thermal conductivities in grains on the order of $\sim 5$ μm. This allows us to verify anisotropy in the thermal conductivity of $\beta$-$Y_2Si_2O_7$ based on EBSD-correlated grain orientation, ultimately yielding a description of the thermal conductivity tensor of the system. In all, this work demonstrates the power of laser-based transient techniques in which thermal conductivity variations at the microstructural level are present in the material system.

We acknowledge the financial support from Materials Research and Design Incorporated, the NASA Small Business Technology Transfer (STTR, Grant No. NNX16CS79C), the National Science Foundation (Grant No. CBET-1706388 and DMR-1921973 through a DMREF program). D.H. Olson is grateful for funding from the National Defense Science and Engineering Graduate (NDSEG) and Virginia Space Grant Consortium (VSGC) Fellowships. We are grateful for discussions with Dr. Sean Agnew of the University of Virginia regarding the EBSD characterization.

## Declaration of Competing Interest

None.

## Supplementary material

Supplementary material associated with this article can be found in the online version at doi:10.1016/j.actamat.2020.02.040

## References

[1] C.H. Liebert, F.S. Stepka, Industry Tests of NASA Ceramic Thermal Barrier Coating, Tech. Rep., Lewis Research Center, 1979.
[2] A.H. Rossette, Z.M.C. A. Demeulenaere, J.A. Roque, L. Hernández, The effect of start-up cycle in ceramic coating used as thermal barrier for a gas turbine bucket, Appl. Therm. En.g 29 (14–15) (2009) 3056–3065, doi: 10.1016/j.applthermaleng.2009.04.011.
[3] D.H. LeMieux, On-line Thermal Barrier Coating (TBC) Monitor for Real-time Failure Protection and Life Maximization, Tech. rep., Siemens Power Generation, Inc, 2005, doi: 10.21611/qirt.2006.043.
[4] M.D. Beals, S. Zerfoss, Volume change attending low-to-high inversion of cristobalite, J. Am. Ceram. Soc. 27 (10) (1944) 285–292, doi: 10.1111/j.1151-2916.1944.tb14471.x.
[5] D.R. Peacor, High-temperature single-study of the cristobalite inversion, Zeitschrift für Kristallographie 138 (1973) 274–298, doi: 10.1524/zkri.1973.138.138.274.
[6] P.J. Heaney, C.T. Prewitt, Silica: Physical Behavior, Geochemistry and Materials Applications, Mineralogical Scoeity of America, 1994.
[7] E.J. Opila, R.E. Hann, Paralinear oxidation of CVD sic in water vapor, J. Am. Ceram. Soc. 80 (1) (1997) 197–205, doi: 10.1111/j.1151-2916.1997.tb02810.x.
[8] E.J. Opila, J.L. Smialek, R.C. Robinson, D.S. Fox, N.J. Jacobson, Sic recession caused by $SiO_2$ scale volatility under combustion conditions: I, thermodynamics and gaseous-diffusion model, J. Am. Ceram. Soc. 82 (7) (1999) 1826–1834, doi: 10.1111/j.1151-2916.1999.tb02004.x.
[9] B.T. Richards, K.A. Young, F. de Francqueville, S. Sehr, M.R. Begley, H.N. Wadley, Response of ytterbium disilicate-silicon environmental barrier coatings to thermal cycling in water vapor, Acta Mater. 106 (2016) 1–14, doi: 10.1016/J.ACTAMAT.2015.12.053.
[10] Y. Arai, Y. Aoki, Y. Kagawa, Effect of cristobalite formation on the delamination resistance of an oxide/Si/(SiC/SiC) environmental barrier coating system after cyclic high temperature thermal exposure, Scr. Mater. 139 (2017) 58–62, doi: 10.1016/j.scriptamat.2017.06.006.
[11] B.T. Richards, M.R. Begley, H.N. Wadley, Mechanisms of ytterbium monosilicate/mullite/silicon coating failure during thermal cycling in water vapor, J. Am. Ceram. Soc. 98 (12) (2015) 4066–4075, doi: 10.1111/jace.13792.
[12] F.W. Zok, Ceramic-matrix composites enable revolutionary gains in turbine engine efficiency, Am. Ceram. Soc. Bull. 95 (5) (2016) 22–28.www.ceramics.org
[13] K.N. Lee, D.S. Fox, N.P. Bansal, Rare earth silicate environmental barrier coatings for SiC/SiC composites and $Si_3N_4$ ceramics, J Eur Ceram Soc 25 (2005) 1705–1715, doi: 10.1016/j.jeurceramsoc.2004.12.013.
[14] Y. Xu, X. Hu, F. Xu, K. Li, Rare earth silicate environmental barrier coatings: present status and prospective, Ceram Int 43 (8) (2017) 5847–5855, doi: 10.1016/J.CERAMINT.2017.01.153.
[15] H.E. Eaton, G.D. Linsey, K.L. More, J.B. Kimmel, J.R. Price, N. Miriyala, EBC protection of SiC/SiC composites in the gas turbine combustion environment, ASME Turbo Expo 2000: Power for Land, Sea, and Air, ASME, 2000, doi: 10.1115/2000-GT-0631.P. V004T02A018

[16] M. Aparicio, A. Durán, Yttrium silicate coatings for oxidation protection of carbon-silicon carbide composites, J. Am. Ceram. Soc. 83 (6) (2004) 1351–1355, doi: 10.1111/j.1151-2916.2000.tb01392.x.
[17] Z. Sun, Y. Zhou, J. Wang, M. Li, Thermal properties and thermal shock resistance of $\gamma$-$Y_2Si_2O_7$, J. Am. Ceram. Soc. 91 (8) (2008) 2623–2629, doi: 10.1111/j.1551-2916.2008.02470.x.
[18] H. Klemm, Silicon nitride for high-temperature applications, J. Am. Ceram. Soc. 93 (6) (2010) 1501–1522, doi: 10.1111/j.1551-2916.2010.03839.x.
[19] K. Fukuda, H. Matsubara, Thermal expansion of $\delta$-yttrium disilicate, J. Am. Ceram. Soc. 87 (1) (2004) 89–92, doi: 10.1111/j.1551-2916.2004.00089.x.
[20] M.D. Dolan, B. Harlan, J.S. White, M. Hall, S.T. Misture, S.C. Bancheri, B. Bewlay, Structures and anisotropic thermal expansion of the $\alpha$, $\beta$, $\gamma$, and $\delta$ polymorphs of $Y_2Si_2O_7$, Powder Diffr. 23 (1) (2008) 20–25, doi: 10.1154/1.2825308.Https://www.cambridge.org/core/services/aop-cambridge-core/content/view/FA6734675D0974755B0F734A6A838F62/S0885715600000609a.pdf/structures_and_anisotropic_thermal_expansion_of_the_and_polymorphs_of_y2si2o7.pdf
[21] N.A. Nasiri, N. Patra, D. Horlait, D.D. Jayaseelan, W.E. Lee, Thermal properties of rare-earth monosilicates for EBC on Si-based ceramic composites, J. Am. Ceram. Soc. 99 (2) (2015) 589–596, doi: 10.1111/jace.13982.
[22] D.R. Clarke, Materials selection guidelines for low thermal conductivity thermal barrier coatings, Surf. Coat. Technol. 163 (2003) 67–74. Https://ac.els-cdn.com/S0257897202005935/1-s2.0-S0257897202005935-main.pdf?_tid=0abf131e-d63c-4d15-a88a-1082800ef81f&acdnat=1538495017_8009fbfe3d19f355d7075ffb5b35ea05
[23] Z. Wu, L. Sun, P. Wan, J. Li, Z. Hu, J. Wang, In situ foam-gelcasting fabrication and properties of highly porous $\gamma$-$Y_2Si_2O_7$ ceramic with multiple pore structures, Scr Mater 103 (2015) 6–9, doi: 10.1016/j.scriptamat.2015.02.024.
[24] Z. Wu, L. Sun, P. Wan, J. Wang, Preparation, microstructure and high temperature performances of porous $\gamma$-$Y_2Si_2O_7$ by in situ foam-gelcasting using gelatin, Ceram Int 41 (2015) 14230–14238, doi: 10.1016/j.ceramint.2015.07.051.www.sciencedirect.com
[25] D.G. Cahill, S.K. Watson, R.O. Pohl, Lower limit to the thermal conductivity of disordered crystals, Phys. Rev. B 46 (10) (1992) 6131–6140, doi: 10.1103/PhysRevB.46.6131.
[26] G.J. Redhammer, G. Roth, $\beta$-$Y_2Si_2O_7$, a new thortveitite-type compound, determined at 100 and 280 k, Acta Crystallogr., Sect. C: Cryst. Struct. Commun. 59 (10) (2003), doi: 10.1107/S0108270103018869.
[27] P.E. Hopkins, J.R. Serrano, L.M. Phinney, S.P. Kearney, T.W. Grasser, C.T. Harris, Criteria for cross-plane dominated thermal transport in multilayer thin film systems during modulated laser heating, J Heat Transfer 132 (8) (2010) 81302, doi: 10.1115/1.4000993.
[28] A.J. Schmidt, X. Chen, G. Chen, Pulse accumulation, radial heat conduction, and anisotropic thermal conductivity in pump-probe transient thermoreflectance, Rev. Sci. Instrum. 79 (11) (2008) 114902, doi: 10.1063/1.3006335.
[29] D.G. Cahill, Analysis of heat flow in layered structures for time-domain thermoreflectance, Rev. Sci. Instrum. 75 (12) (2004) 5119–5122, doi: 10.1063/1.1819431.
[30] J.P. Feser, D.G. Cahill, Probing anisotropic heat transport using time-domain thermoreflectance with offset laser spots, Rev. Sci. Instrum. 83 (2012) 104901, doi: 10.1063/1.4757863.
[31] J.P. Feser, J. Liu, D.G. Cahill, Pump-probe measurements of the thermal conductivity tensor for materials lacking in-plane symmetry, Rev. Sci. Instrum. 85 (10) (2014) 104903, doi: 10.1063/1.4897622.
[32] D. Rodin, S.K. Yee, G.W. Woodruff, Simultaneous measurement of in-plane and through-plane thermal conductivity using beam-offset frequency domain thermoreflectance, J. Appl. Phys. 88 (2017) 14902, doi: 10.1063/1.4973297.http://aip.scitation.org/toc/rsi/88/1
[33] P. Jiang, X. Qian, R. Yang, A new elliptical-beam method based on time-domain thermoreflectance (TDTR) to measure the in-plane anisotropic thermal conductivity and its comparison with the beam-offset method, Rev. Sci. Instrum 89 (9) (2018), doi: 10.1063/1.5029971.
[34] M. Li, J.S. Kang, Y. Hu, Anisotropic thermal conductivity measurement using a new asymmetric-beam time-domain thermoreflectance (AB-TDTR) method, Rev. Sci. Instrum. 89 (2018) 84901, doi: 10.1063/1.5026028. http://aip.scitation.org/toc/rsi/89/8
[35] C. Wei, X. Zheng, D.G. Cahill, J.C. Zhao, Invited article: micron resolution spatially resolved measurement of heat capacity using dual-frequency time-domain thermoreflectance, Rev. Sci. Instrum. 84 (2013) 71301, doi: 10.1063/1.4815867.
[36] P. Jiang, X. Qian, R. Yang, Tutorial: time-domain thermoreflectance (TDTR) for thermal property characterization of bulk and thin film materials, J. Appl. Phys. 124 (16) (2018) 161103, doi: 10.1063/1.5046944.
[37] A. Sood, R. Cheaito, T. Bai, H. Kwon, Y. Wang, C. Li, L. Yates, T. Bougher, S. Graham, M. Asheghi, M. Goorsky, K.E. Goodson, Direct visualization of thermal conductivity suppression due to enhanced phonon scattering near individual grain boundaries, Nano Lett. 18 (6) (2018) 3466–3472, doi: 10.1021/acs.nanolett.8b00534. https://pubs.acs.org/sharingguidelines
[38] R.E. Newnham, Properties of materials: Anisotropy, symmetry, structure, Oxford University Press USA - OSO, Oxford, United Kingdom, 2004. http://ebookcentral.proquest.com/lib/uva/detail.action?docID=422681
[39] A. Einstein, Über die von der molekularkinetischen theorie der wärme geforderte bewegung von in ruhenden flüssigkeiten suspendierten teilchen, Ann Phys 322 (8) (1905) 549–560, doi: 10.1002/andp.19053220806.
[40] Z. Tian, L. Zheng, Z. Li, J. Li, J. Wang, Exploration of the low thermal conductivities of $\gamma$-$Y_2Si_2O_7$, $\beta$-$Y_2Si_2O_7$, $\beta$-$Yb_2Si_2O_7$, and $\beta$-$Lu_2Si_2O_7$ as novel environmental barrier coating candidates, J. Eur. Ceram Soc. 36 (11) (2016) 2813–2823, doi: 10.1016/J.JEURCERAMSOC.2016.04.022.
[41] J.W. Jaeken, S. Cottenier, Solving the christoffel equation: phase and group velocities, Comput. Phys. Commun. 207 (2016) 445–451, doi: 10.1016/j.cpc.2016.06.014.
[42] Synthesis of $\beta$-$Y_2Si_2O_7$ nanowires via a facile molten salt method and their thermal properties, J. Alloys Compd. 699 (2017) 210–215, doi: 10.1016/j.jallcom.2016.12.305.